Optimal Trajectory Generation for a Quadrotor Biplane Tailsitter

Kristoff McIntosh
Graduate Student
Rensselaer Polytechnic Institute
Troy, NY, USA

Jean-Paul Reddinger
Aerospace Engineer
CCDC Army Research Laboratory
Aberdeen Proving Ground, MD, USA

Di Zhao
Ph.D. Candidate
Rensselaer Polytechnic Institute
Troy, NY, USA

Sandipan Mishra
Associate Professsor
Rensselaer Polytechnic Institute
Troy, NY, USA

ABSTRACT

This paper introduces a methodology for an optimization-based trajectory planner for the autonomous transition of a quadrotor biplane tailsitter (QRBP) between the flight modes of hover to forward flight and forward flight to hover. The trajectory planner uses a simplified first principles dynamic model of the QRBP in the formulation of a optimization problem for trajectory planning. Additional constraints on the trajectory are imposed based on physical limitations, such as available power, stall limits, among others. The cost function for the optimization problem is chosen to be the time-of-transition. The solution of this problem generates time-optimal state and input trajectories for transition. To validate the algorithm, the trajectories are tested on a flight dynamics simulation of a QRBP to demonstrate feasibility and tracking performance with an inner-loop PID feedback controller; and compared against trajectories generated from a heuristic approach. The results of the simulated tracking performance indicate the proposed trajectory planner is capable of generating feasible transition trajectories for the previously specified flight modes.

NOTATION

x	*inertial position forward*
z	*inertial altitude*
V	*inertial velocity*
γ	*flight path angle*
V_w	*rotor wake velocity*
V_a	*airspeed*
α	*geometric angle of attack (wing)*
α_e	*effective angle of attack (wing)*
ϕ	*pitch angle*
L	*lift*
D	*drag*
T	*thrust*
ρ	*air density (sea level)*
R	*rotor disk radius*
C_{L_0}	*lift curve intercept*
C_{L_a}	*lift curve slope*
C_{D_0}	*drag curve intercept*
S_l	*aerodynamic wing area*
S_d	*aerodynamic fuselage area*
m	*mass of CRC* $-$ 20
g	*gravitational acceleration constant*

INTRODUCTION

Transitioning Unmanned Aerial Systems (UAS) are a class of aerial vehicles that are capable of different modes of flight, such as vertical takeoff and landing rotorcraft as well as fixed wing forward flight. These hybrid aircraft are specifically designed to capitalize on the strengths of their different modes of flight, such as combining electrically powered vertical take-off and landing (e-VTOL) vehicles in hover and climb, with the efficiency of fixed wing aircraft in forward flight. Such UAS are capable of high degrees of maneuverability, reduced take-off and landing footprint, increased endurance in hover, and larger capacity for payload delivery, and thus are of particular interest for both civilian (Ref. 1) and military applications (Ref. 2).

As a result, there has been significant progress towards development of transitioning UAS designs, such as the Quadrotor Biplane (QRBP) design described in (Ref. 3) and the eV-bat and Y-bat designs described in (Ref. 4). The CCDC Army Research Laboratory (ARL), in conjunction with the University of Maryland, has developed a series of hybrid UAS research vehicles, modeled after the QRBP. This series of UAS was designed to further develop understanding of the vehicle's operation from an aeromechanics, propulsion, and autonomous control standpoint, as the vehicle is scaled in size and weight. These vehicles are collectively known as the Common Research Configuration (Refs. 5, 6). The vehicle used in this study is the 20-lb Common Research Configuration (CRC-20), shown in Figure 1.

One of the challenges in autonomy for transitioning UAS is the development of effective guidance, navigation, and control strategies, particularly for the transition between hover/ascent and forward flight modes. Several efforts regarding the gen-

Presented at the VFS International 76th Annual Forum & Technology Display, Virginia Beach, Virginia, Oct 6–8, 2020.

Figure 1. CRC-20 Research QRBP

eral autonomous flight control of transitioning UAS have been made in the past decade. For example, in (Ref. 7), Todeschini employed a model-based hierarchical control strategy for a hybrid drone wind energy system, where they developed a switching strategy for transitioning between hover and forward flight. Raj *et al* (Ref. 8) employs a PD controller on the pitching moment acting on a QRBP with a swiveling to yaw control authority. Chipade *et al* (Ref. 9) applied a PID feedback controller on a QRBP and enabled stabilization and small angle tracking during a hover test. In (Ref. 10), a cascaded control methodology was designed by Nogar *et al* for a hybrid vehicle with dual tilting rotors, and the backstepping technique was used for converting control forces and moments into actuator inputs, which eventually achieved flights with large body rotation. Hrishikeshavan *et al* (Ref. 11) applied a quaternion-based method on a micro QRBP air vehicle, which was proved to be capable of transitioning from hover to forward flight by simulation, bench-top experiment, and free flight test. Similarily, Swarnkar *et al* (Ref. 12) uses a quaternion-based framework for attitude representation of a micro QRBP control architecture, which achieved both hover to forward flight transition and vice versa.

While the above efforts have concentrated on developing robust inner-loop control laws for transition from hover to forward flight of the hybrid aerial vehicles and vice versa, the outer-loop trajectory for transition is typically generated heuristically, usually by generating simple profiles of the position and velocity variables (Ref. 7) or determined by a human pilot (Ref. 1). Although these trajectories normally can be tracked by micro hybrid vehicles since they are over-powered, these methods may fail in application to larger vehicles, which have less control authority and stringent constraints on the flight states due to a general reduction in maximum thrust-to-weight ratio, resulting in tighter power and stall limitations (Ref. 5, 13). The larger eVTOL industry is particularly interested in this scalability issue. [1].

[1]The aerospace corporation Bell in Forth Worth, TX developed a transitioning UAS. The vice president cites that while "general flight procedures are very well understood..." for larger vehicles, "you must be careful about power management, speed, and how much altitude you will gain or lose..." during transition (Ref. 14).

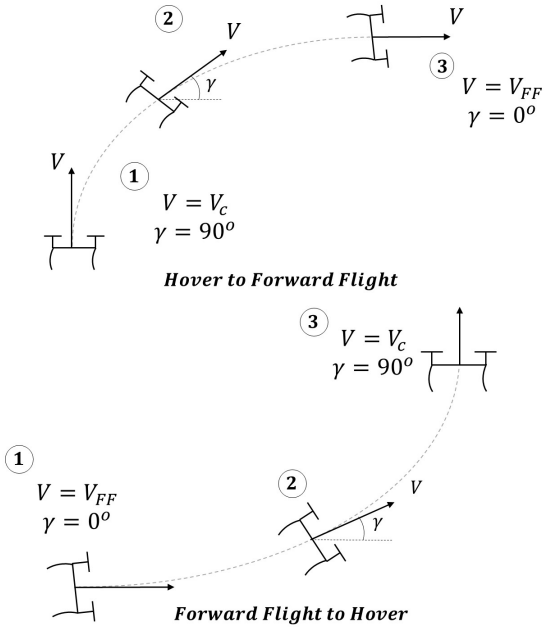

Figure 2. Description of Transition Problem.

Therefore, this paper seeks to develop a general model-based approach to deriving (time optimal) guidance trajectories for the autonomous transition of the CRC-20 between flight modes (hover to forward-flight and vice-versa). The proposed algorithm for trajectory generation is validated and shown to be capable of guiding the CRC-20 through the transition for a variety of initial and terminal flight states, while conforming to physical constraints such as power and stall limits. Finally, these trajectories are shown to be successfully deployed on a flight dynamics simulation model of the CRC-20, similar to the one described in (Ref. 5).

PROBLEM STATEMENT

The scope of this paper will be limited to the design of the trajectory planner, whose purpose is to generate the state trajectories $x^*(.)$ and input trajectories $u^*(.)$ for subsequent inner loop control. The typical guidance/navigation/control architecture to provide inner loop control of the CRC-20 consisting of four SISO PID control loops ($v \rightarrow u_{COLL}$, $\theta \rightarrow u_{LATR}$, $\phi \rightarrow u_{LNGL}$, and $\psi \rightarrow u_{PEDL}$; to be elaborated in the results section). The control architecture is briefly described in Figure 3).

Given an initial flight condition x_0 and a final flight condition x_f (e.g. hover to forward flight), the goal is to generate the necessary state and input trajectories ($x^*(.)$ and $u^*(.)$, respectively), that will allow a QRBP to transition between x_0 and x_f, subject to the vehicle's dynamic and design constraints. Figure 2 shows a visualization of the transition problem, where the planned path for the trajectories lies in a 2-dimensional plane ($x-z$ plane). Thus, the inertial position x, z, the inertial velocity V, and the flight path angle γ are sufficient to describe the transition.

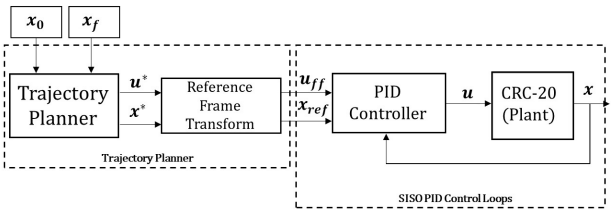

Figure 3. General Control Architecture.

This paper proposes an optimization-based approach for the generation of $x^*(.)$ and $u^*(.)$, as below:

$$\begin{aligned} \underset{x,\,u}{\arg\min} \quad & J = f(x,u,t), && \textit{cost function} \\ s.t \quad & \dot{x} = \mathbf{f}(x,u), && \textit{dynamics constraints} \\ & x(t_0) = x_0, && \textit{initial state constraint} \\ & x(t_f) = x_f, && \textit{terminal state constraint} \\ & x \in \mathbf{X} \;\; u \in \mathbf{U}, && \textit{state and input constraints} \end{aligned} \tag{1}$$

In order to formulate and solve this problem, (1) a suitable model for the dynamics during transition is developed, (2) suitable constraints are designed for enforcing physical limitations such as power and stall, and (3) a numerical approach is constructed to solve this optimization problem in a computationally tractable manner. The following sections expand on these steps. Upon generation, the trajectories must be trackable using a typical guidance/navigation/control architecture, described in Figure 3. A flight dynamics simulation model of the CRC-20, designed by CCDC-ARL (Ref. 5), is used for simulated testing of the trajectory generation algorithm.

SIMPLIFIED DYNAMICAL MODEL

This section presents a suitable model of the dynamics of the CRC-20 in transition between flight modes for trajectory planning. Note that in contrast to the aerodynamic model of the CRC-20 described in Ref. 5, this model must be a reasonably accurate yet low order simplified expression of the vehicle dynamics for computational efficiency of the solution to the optimization problem. Thus, the model must accurately capture the behavior of the vehicle in transition, while being sufficiently simple for use in a discrete optimal control approach to trajectory planning. To accomplish this goal, a modeling approach based on the one found in Ref. 15 is used, which describes the dynamics of a fixed wing aircraft as a point mass in the wind frame.

Frames of Reference: To model the dynamics of the CRC-20 in transition, the following frames of reference to capture the vehicle's state are defined (as shown in Fig. 4). $\hat{i}$: a conventionally defined inertial reference frame whose origin is fixed at an arbitrary point in space; $\hat{b}$: a conventionally defined body reference frame with origin fixed at the vehicle center of mass; and finally, $\hat{c}$: a wind frame defined by the direction of the vehicle freestream velocity vector, V_i (which is tangential to the flight path). To account for aerodynamic interference effects from the rotor on the wing, a modified wind reference frame $\hat{e}$ is established to describe the aerodynamic forces acting on the wing. This reference frame is governed by the direction of the the modified velocity vector V_a, which is defined in the next section. These four reference frames, $\hat{i},\hat{b},\hat{c}$, and $\hat{e}$ allow us to express the dynamics of the QRBP in any reference frame we deem convenient.

Dynamical Model

To determine the magnitude of the aerodynamic forces acting on the CRC-20 during transition, the effect of the rotor wake impinging on the wings must be accounted. The rotor wake velocity vector, V_w, is scaled and added to the freestream velocity experienced by the wing, V_i. The magnitude of the wake velocity is a function of the rotor thrust, derived using the momentum theory-based interference model from Ref. 5 with $\eta = 0.6$. For this model, we assume V_w is always orthogonal to the rotor plane, and is thus always aligned along $\hat{b}_1$. The resulting velocity vector affecting the wing (V_a) increases the dynamic pressure on the wing and modifies the wing angle of attack (α_e). These modified parameters allow for a more accurate model-based expression of the aerodynamic forces L and D acting on the QRBP.

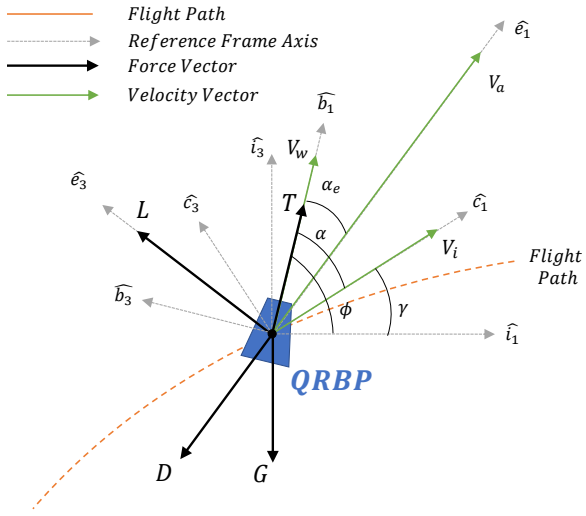

Figure 4. Reference Frames and Free Body Diagram

Since the dominant effects of V_i and V_w are expected to change significantly during transition, this model is necessary for the accurate calculation of the aerodynamic forces as a function of time.

For the purposes of this paper, we make the assumption that any transition made by the QRBP occurs in a $2D$ plane (say, the $x-z$ plane). This limits the vehicle to translational motion in the inertial $x-z$ plane and rotational motion about the inertial y-axis. Since the transition is modeled in a $2D$ plane, four states are needed to define the dynamics of the vehicle, namely the translational motion in x and z, the vehicle

freestream velocity V_i and the flight path angle γ. Assuming knowledge of the state variables, and take the inputs to the vehicle to be the vehicle thrust T and pitch angle ϕ; V_w, V_a, α_e and the aerodynamic forces can be defined as shown in Table 1 (Note that α represents the wing angle of attack of the vehicle w.r.t to V_i and α_e is the effective wing angle of attack due to rotor downwash).

Table 1. Expressions for angles, velocities, and forces.

Variable (Angle/ Velocity/Force)	Expression
Angle of attack α	$\phi - \gamma$
Effective angle of attack α_e	$\arcsin \frac{V_i \sin\alpha}{V_a}$
Wake velocity V_w	$1.2\sqrt{\frac{T}{8\rho\pi R^2}}$
Air speed V_a	$\sqrt{V_i^2 + V_w^2 + 2V_iV_w\cos\alpha}$
Lift Force L	$0.5\rho(C_{L0} + C_{L\alpha}\alpha_e)S_l V_a^2$
Drag Force D	$0.5\rho C_{D0} S_d V_a^2$

From here, we derive the dynamic equations of motion using simple trigonometry. Note that these equations operate under the assumption that the vehicle is a point mass; thus these equations do not accurately model the rotational inertia of the vehicle. Also note that the variables $x, z, V_i, \gamma, T, \phi, L$, and α_e are all functions of time.

$$\begin{aligned} \dot{x} &= V_i\cos\gamma \\ \dot{z} &= V_i\sin\gamma \\ \dot{V}_i &= \frac{T\cos\alpha - L\sin(\alpha-\alpha_e) - D\cos(\alpha-\alpha_e)}{m} - g\sin\gamma \\ \dot{\gamma} &= \frac{T\sin\alpha + L\cos(\alpha-\alpha_e) - D\sin(\alpha-\alpha_e)}{mV_i} - \frac{g\cos\gamma}{V_i} \end{aligned} \tag{2}$$

These equations represent the dynamic constraints $\dot{\mathbf{x}} = \mathbf{f}(\mathbf{x},\mathbf{u})$ of the vehicle to be employed in the trajectory generation optimization problem, s.t. $\mathbf{x} = [x\ z\ V\ \gamma]^T$, and $\mathbf{u} = [T\ \alpha]^T$.

TRAJECTORY GENERATION: OPTIMIZATION PROBLEM

Cost Function and Decision Variables Here, the optimization problem for generating time-optimal trajectories is formulated based on method described in (Ref. 16). The objective function is chosen to be $J = t_f - t_0$, i.e., we wish to minimize the total time of flight for the transition. The decision variables for the optimization problem are the state $\mathbf{x}(\cdot)$ and input $\mathbf{u}(\cdot)$ trajectories described previously. The solution of this problem generates the optimal state and input trajectories $\mathbf{x}^*(\cdot)$ and $\mathbf{u}^*(\cdot)$ that serve as the reference and feedforward signals for the inner loop.

Dynamics Constraints The dynamics constraints on the vehicle are the dynamical equations derived from the point mass model described in Eqn. 2. These dynamics are expressed in discrete-time form. The dynamics derived from the point mass model are discretized using trapezoidal differentiation with a variable time step T, producing a discrete dynamic equation of the following form:

$$\begin{aligned} &\mathbf{x}(k+1) = \mathscr{F}(\mathbf{x}(k),\mathbf{u}(k)), \text{where} \\ &\textit{where}: \\ &\mathscr{F}(\mathbf{x}(k),\mathbf{u}(k)) = \mathbf{x}(k) + \\ &\tfrac{kT}{2}(\mathbf{f}(\mathbf{x}(k),\mathbf{u}(k)) + \mathbf{f}(\mathbf{x}(k+1),\mathbf{u}(k+1)) \end{aligned} \tag{3}$$

Boundary Constraints The boundary constraints are the initial and final states of the maneuver. For this problem, we constrain the initial state to an exact location, while setting a tolerance on the final state, such that: $\mathbf{x}(k_0 T) = \mathbf{x}_0$, and $\|\mathbf{x}(k_f T) - \mathbf{x}_f\| < \varepsilon$.

Power/Stall Constraints The power ceiling P_{max} and stall angle α_{stall} of the QRBP place additional constraints on state trajectories for the vehicle. To account for this, any optimal trajectory generated for the aircraft to transition between flight modes must not exceed the specified stall angle or power limit (Ref. 5). Thus, path constraints are placed on the power P and α_e to remain within power and stall limits.

$$\begin{aligned} &\alpha_e \le \alpha_{stall} - \varepsilon_{\alpha_{tol}} \\ &P(T) \le P_{max} \qquad \textit{where} \quad P(T) = T\Omega R\tfrac{C_Q}{C_T} \end{aligned} \tag{4}$$

where T is the total thrust produced by the rotors, C_Q and C_T are the power and thrust coefficients of the rotors, respectively, and Ω, R are the rotational speed and radius of a single rotor, respectively. $\varepsilon_{\alpha_{tol}}$ is a safety factor placed on the stall constraint as added preventative measure against stall during tracking. Note that P_{max} and α_{stall} are 2.01 hp and 13.5^o, respectively.

Constraints on Inertial Acceleration and Pitch Rate As previously stated, the dynamical equations of motion used in the trajectory generation scheme do not capture the inertia of the vehicle. Therefore, in order to prevent the trajectory from expecting the aircraft to perform accelerations that are impossible to track, it is necessary to impose path constraints on the vehicle acceleration $\dot{V}_i$ and pitch rate $\dot{\phi}$. Any trajectory generated for the aircraft to transition between flight modes must stay within a specified limit of inertial acceleration or pitch rate.

$$\begin{aligned} \dot{V}_{i_{min}} \le \dot{V} \le \dot{V}_{i_{max}} \\ \dot{\phi}_{min} \le \dot{\phi} \le \dot{\phi}_{max} \end{aligned} \tag{5}$$

Trajectory Optimization Problem Formulation In summary, the optimization problem for transitioning UAS trajectory generation takes the following form:

$$\begin{aligned} \underset{\mathbf{x},\,\mathbf{u}}{\arg\min} \quad & J = f(x,u,k) \\ s.t \quad & \mathbf{x}(k+1) = \mathscr{F}(\mathbf{x}(k),\mathbf{u}(k)) \\ & \mathbf{x}(k_0 T) = \mathbf{x}_0 \\ & \mathbf{x}(k_f T) = \mathbf{x}_f \\ & \mathbf{x}(k) \in \mathscr{X} \quad \mathbf{u}(k) \in \mathscr{U} \end{aligned} \tag{6}$$

where the cost function J is used to determine the parameter of the trajectory that will be optimized (e.g. time-optimal $[t_f - t_0]$, power optimal $[\sum_k u^2(k)]$, etc.). Note that $\mathscr{X}$ and $\mathscr{U}$ represent the feasible set of allowable states and inputs, respectively, defined by all other previously mentioned path constraints. The gradient-based optimization solver tool CasADi was used to implement the optimization problem for trajectory generation (Ref. 17).

RESULTS

An analysis of the trajectory planning algorithm will now be presented. First, heuristic transition trajectories for each flight case (hover to forward flight and vice versa) are designed and assessed in simulation. Then, time-optimal transition trajectories ($J = t_f - t_0$) are produced by the optimizer with the heuristic trajectories serving as an initial guess. The performance of both trajectories are then compared, both in terms of controller tracking performance and established design constraints ($P, \alpha_e, \dot{V}_i, \dot{\gamma}$, etc.).

Simulation Setup and Controller Design

All generated transition trajectories (both heuristic and optimal) are simulated on the closed loop system consisting of a flight dynamics model of the CRC-20 derived from empirical generated in Flight Lab (refer to Ref. 5) with a feedback inner loop control architecture consisting of a PID controller.

The state of the vehicle is described by the conventional 12-D model for a VTOL aircraft ($\mathbf{x} = [x\ y\ z\ \phi\ \theta\ \psi\ u\ v\ w\ p\ q\ r]^T$). A change of basis was performed on the optimal trajectories to preserve continuity. The CRC-20's four inputs $\mathbf{u} = [u_{COLL}\ u_{LATR}\ u_{LNGL}\ u_{PEDL}]_T$ are linearly concatenated versions of the four rotor's rotational speeds $[\Omega_1\ \Omega_2\ \Omega_3\ \Omega_4]^T$ that correspond to the longitudinal body velocity of the vehicle v and the attitude of the vehicle in three dimensions (ϕ, θ, ψ representing vehicle pitch, roll, and yaw angles). The relationship between these is:

$$\begin{bmatrix} u_{COLL} \\ u_{LATR} \\ u_{LNGL} \\ u_{PEDL} \end{bmatrix} = \frac{1}{4} \begin{bmatrix} 1 & 1 & 1 & 1 \\ -1 & 1 & 1 & -1 \\ -1 & -1 & 1 & 1 \\ -1 & 1 & -1 & 1 \end{bmatrix} \begin{bmatrix} \Omega_1 \\ \Omega_2 \\ \Omega_3 \\ \Omega_4 \end{bmatrix} \tag{7}$$

For inner loop control design, it was assumed that the effects of coupling between these states is negligible. Thus the control architecture consists of 4 parallel SISO control loops, which are described next.

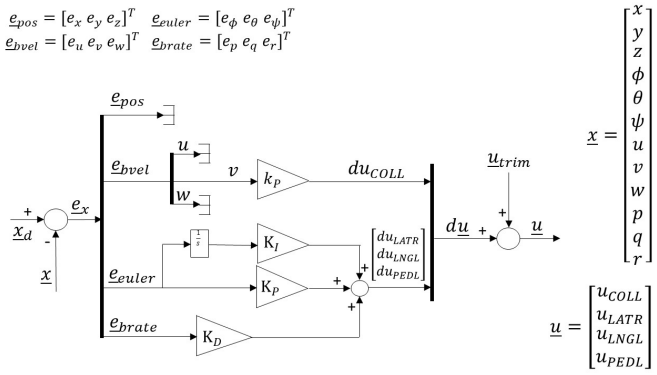

Figure 5. Inner Loop Control Architecture.

The controller used for simulation was a series of PID compensators acting on the four control loops corresponding to four SISO systems, $v \rightarrow u_{COLL}$, $\theta \rightarrow u_{LATR}, \phi \rightarrow u_{LNGL}$, and $\psi \rightarrow u_{PEDL}$. The controller structure is shown in Figure 5. The controller on $v \rightarrow u_{COLL}$ loop was a simple P compensator with a gain $K_P = 250$. The controller for the remaining loops, $\phi \rightarrow u_{LATR}, \theta \rightarrow u_{LNGL}, \psi \rightarrow u_{PEDL}$ were all PID compensators with the following gains: $[K_P = 0.087,\ K_I = 1,\ K_D = 60]$, $[K_P = 1440,\ K_I = 1,\ K_D = 60]$, and $[K_P = 0.087,\ K_I = 1,\ K_D = 30]$, respectively. This series of PID compensators was used to track the all transition trajectories described in the following section.

Hover to Forward Flight Transition

All generated trajectories (both heuristic and optimal) for the hover to forward flight case begin from a state of initial ascent, with the freestream velocity $V_i = 5.05\ ft/s\ (3\ kts)$ and the flight path angle $\gamma = 90^o$ before beginning the transition to a forward flight state with $V_i = 42.18\ m/s\ (25\ kts)$ and $\gamma = 0^o$. The process for generating the heuristic trajectories and their tracking performance is described in the following section.

Heuristically Designed Trajectories and Tracking Performance Figure 6 shows the heuristically generated trajectories for the hover to forward flight case. These trajectories were generated in the $\hat{c}$ wind reference frame by specifying a desired constant $\dot{\gamma}$ and linearly interpolating between the desired initial ($\gamma_0 = 0\,\text{deg}$) and terminal $\gamma_f = 90\,\text{deg}$ flight path angles to determine the flight time for transition. The inertial velocity (V_i) profile was also determined through linear interpolation between flight states w.r.t. the resulting flight time. The position state profiles $x(\cdot)$ and $z(\cdot)$ were then derived using Eqn. 2. The case where $\dot{\gamma} = 28.125\ deg/s$, with a resulting time of flight of 3.2s is illustrated in this paper (this constraint was chosen so as to not violate the power constraint).

Figures 7 and 8 show the implicit ($\hat{c}$ reference frame) and explicit (body reference frame) tracking performance of the heuristically designed trajectories for the hover to forward flight case. Figure 9 shows the power P and effective wing angle of attack α_e throughout the transition. Referring to Figures 7 and 8, it can be seen that while the controller is tracking

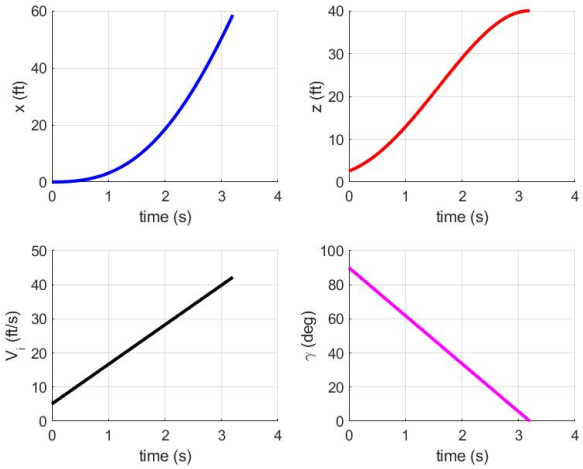

Figure 6. Heuristically Designed Trajectories (Wind Frame): Hover to Forward Flight Case.

v and ϕ with minimal error, there is a significant amount of steady state error (around 9 ft) in z after the transition.

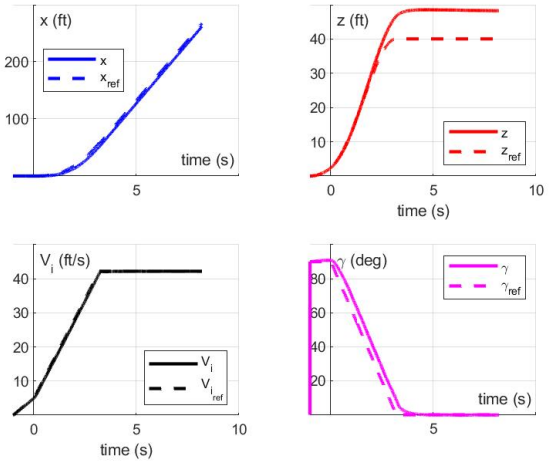

Figure 7. Tracking Performance of Heuristically Designed Trajectories (Wind Frame): Hover to Forward Flight Case.

From Figure 9, it can be seen that this transition stays within the stall boundary, as the absolute value of α_e never exceeds 4^o. However, this trajectory requires the maximum allowable power (2.01 hp) to be sufficiently executed, leaving no factor of safety for power consumption. This suggests that this transition may be impractical to implement on the actual vehicle.

Optimal Trajectories and Tracking Performance The time optimal trajectories (shown in Figure 10) were generated from the optimization-based trajectory planner described in the previous section, using the heuristic trajectories as the initial guess, with several key parameters serving as the path constraints. Specifically, along with the previously specified power and stall path constraints (2.01hp and $\pm 13.5^o$, respectively), the specified $\dot{\gamma}$ as well as the maximum inertial acceleration $\dot{V}$ from the heuristic trajectory were used as constraints in the optimizer ($\pm 30^o/s$ and ± 11.05 ft/s^2, respectively). This resulted in an optimal time of flight of 3.38s.

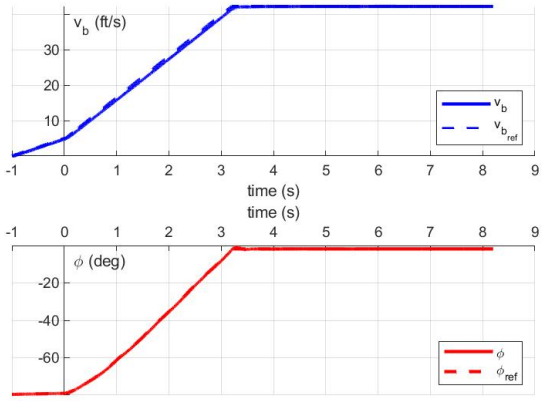

Figure 8. Tracking Performance of the Heuristically Designed Trajectories (Body Frame): Hover to Forward Flight Case.

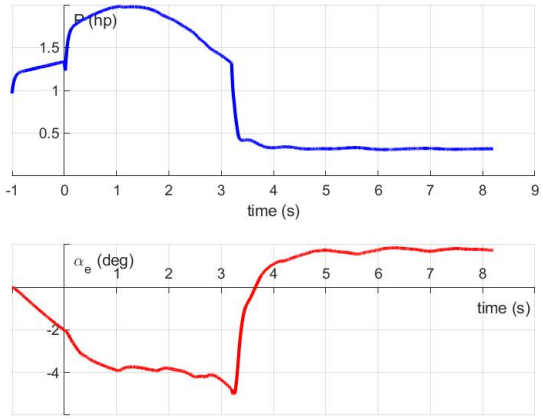

Figure 9. Power/Stall Profiles for Heuristically Designed Trajectories: Hover to Forward Flight Case.

Figure 11 shows the optimal thrust and pitch angle profiles generated by the optimizer, while Figure 12 shows the optimal power and effective wing angle of attack profiles generated by the optimizer. The small oscillations in the trajectories are artifacts from the numerical solution of the optimization problem.

Figures 13 and 14 show the implicit wind frame and explicit body frame tracking performance for the optimal trajectories, respectively. Figure 15 shows the power and effective wing angle of attack profiles of the optimal trajectory in simulation.

From Figure 12, it can be seen that power is the primary active constraint that determines the shape of the trajectory, as the optimizer projects that the vehicle will require the maximum allowable power available to transition from hover to forward flight. The power profile from Figure 15 appears to

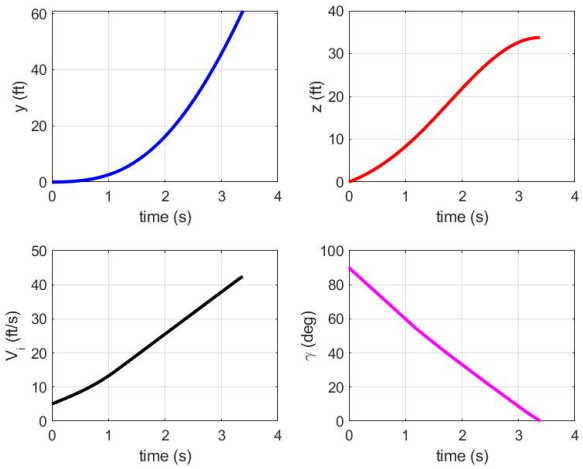

Figure 10. Time Optimal Trajectories (Wind Frame): Hover to Forward Flight Case.

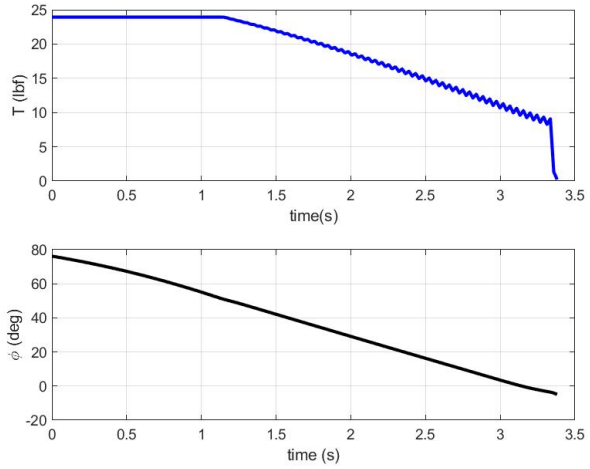

Figure 11. Prescribed Thrust and Pitch Angle Profiles for Time-Optimal Trajectories: Hover to Forward Flight Case.

corroborate this fact, as the power of the vehicle is very close to the maximum power, and is highest during the transition.

Remark: It is important to note that the prescribed power derived from the optimizer does not match the power generated in simulation; this is likely due the fact that the optimizer does not take longitudinal differences in the thrust into account. Consequently in tracking, longitudinal control inputs result in higher power requirements. It is also important to note the high-frequency numerical oscillations that appear in the prescribed power and α_e profiles, which can be addressed by adding suitable regularization to the optimization problem.

Forward Flight to Hover Transition

All generated trajectories for the forward flight to hover case begin from a state of forward flight, with the free-stream velocity $V_i = 42.18\ ft/s\ (25\ kts)$ and the flight path angle $\gamma = 0^o$ before beginning the transition to a forward flight state with

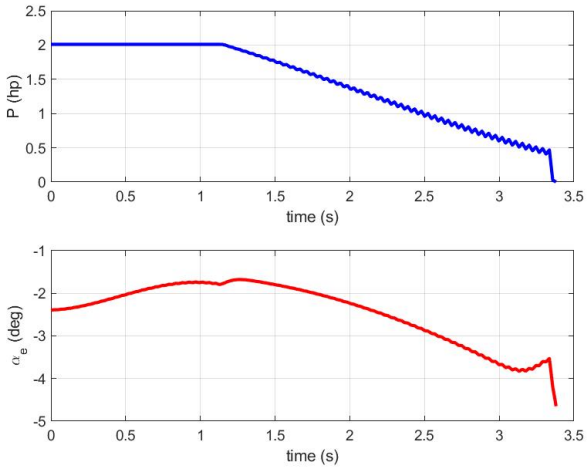

Figure 12. Prescribed Power and Stall Angle Profiles for Time-Optimal Trajectories: Hover to Forward Flight Case.

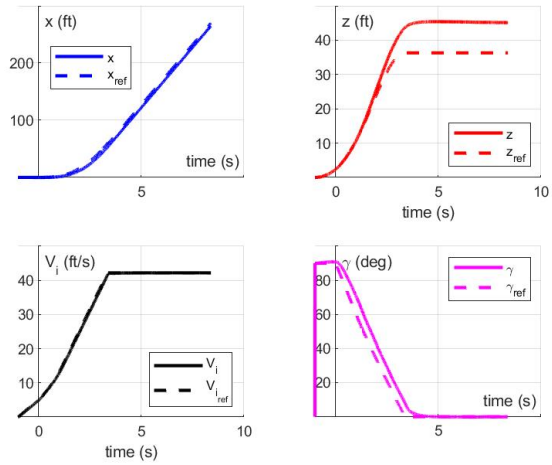

Figure 13. Tracking Performance of Time-Optimal Trajectory (Wind Frame): Hover to Forward Flight Case.

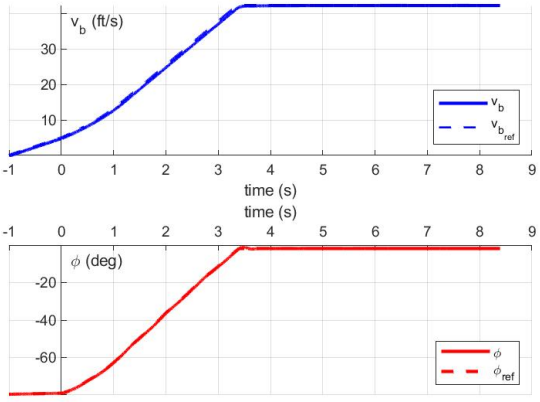

Figure 14. Tracking Performance of Time-Optimal Trajectories (Body Frame): Hover to Forward Flight Case.

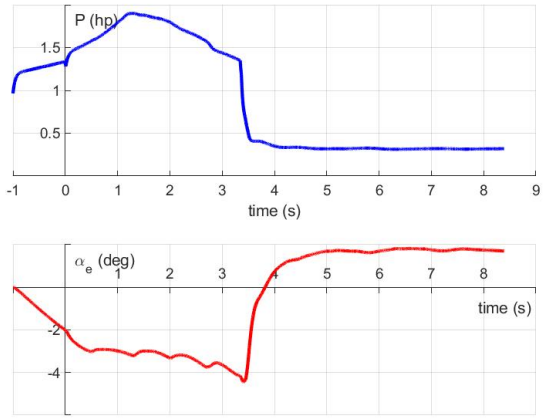

Figure 15. Power/Stall Profiles for Time-Optimal Trajectories: Hover to Forward Flight Case.

$V_i = 5.05\ ft/s\ (3\ kts)$ and $\gamma = 90^o$. Furthermore, the requirement that the terminal height after transition be lower than the initial height at the beginning (during forward flight), by a specified amount is imposed. Thus, the following procedures and analysis reflect that aspect of the transition. The process for generating the heuristic trajectories and their tracking performance is described in the following section.

Heuristic Trajectories and Tracking Performance Similar to the hover to forward flight case, the heuristic trajectories for the forward flight to hover case are generated by careful scheduling of the V and γ, then using Eqn. 2 to determine the x and z profiles. Since a terminal descent was desired for the optimal transition between forward flight and hover, the heuristic profiles were scheduled such that the vehicle follows a very specific flight path. Specifically, the CRC-20 flies down, maintains a short period of level flight, then flies up to a lower position at hover. Figure 16 shows the heuristic trajectories for the forward flight to hover case in the wind frame.

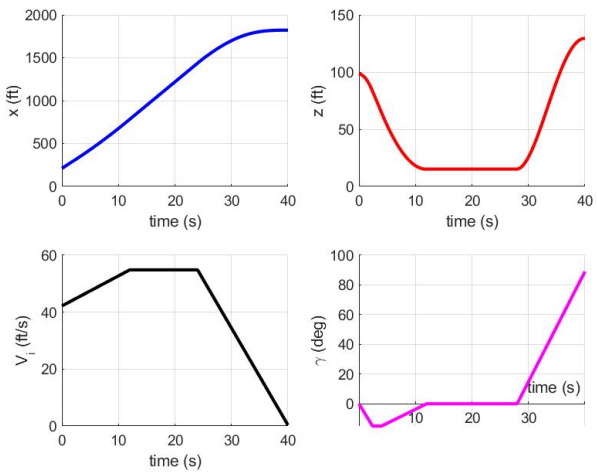

Figure 16. Heuristically Designed Trajectories (Wind Frame): Forward Flight to Hover Case.

Note that the terminal height requirement was not satisfied for the heuristic trajectories, a consequence of the $\dot{V}$ and $\dot{\gamma}$ chosen for the final ascent of the transition. While not ideal, the heuristic trajectory was designed with the desired flight path in mind. Thus, the terminal descent would be managed by the optimizer.

Figures 17 and 18 show the tracking of the trajectories in the wind frame and body frame, respectively. Figure 19 shows the P and α_e profiles. Note that the time of flight for the heuristic trajectory is 40s, which was the shortest time in which the vehicle could complete this maneuver using linear interpolation between flight states (specifically the final ascent towards the end; attempting an upward flight path from a forward flight position while dropping speed is difficult to do quickly).

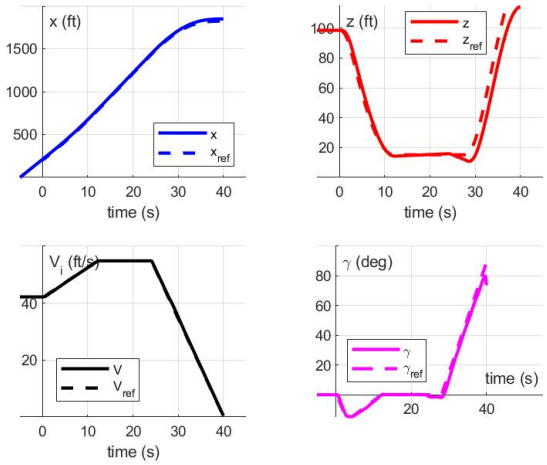

Figure 17. Tracking Performance of Heuristically Designed Trajectories (Wind Frame): Forward Flight to Hover Case.

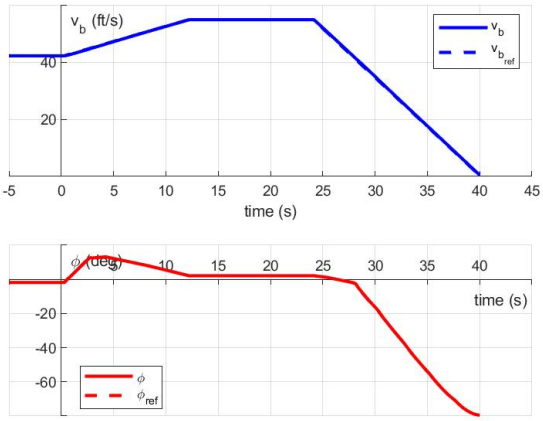

Figure 18. Tracking Performance of Heuristically Designed Trajectories (Body Frame): Forward Flight to Hover Case.

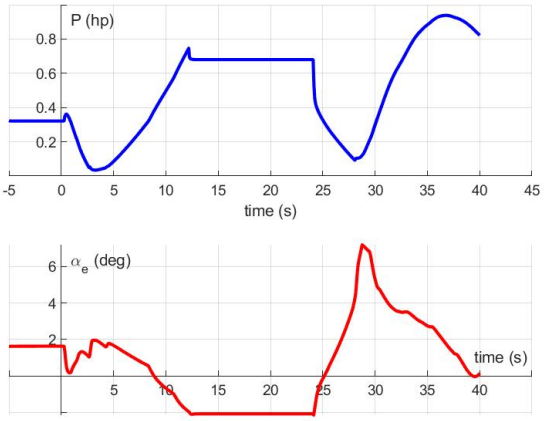

Figure 19. Power/Stall Profiles for Heuristically Designed Trajectories: Forward Flight to Hover Case.

Optimal Trajectories and Tracking Performance As with the optimal trajectories for the hover to forward flight case, the generated heuristic trajectories were used as the initial guess for the optimizer to generate the optimal forward flight to hover trajectory. Furthermore, several constraints were modified in order to generate this trajectories for this transition. First, the lower limit on the decision variable thrust T was decreased into the negative range in order to allow the optimizer to simulate up-wash through the rotors during descent (which would result in a negative thrust from the rotor blades). Second, the design considerations for maximum allowable $\dot{V}$ and $\dot{\gamma}$ for the heuristic trajectories were used as path constraints for the optimizer. Finally, the terminal altitude was constrained to a location 10 m below the starting point (within a small range). These constraints produced the trajectories shown in Figure 20.

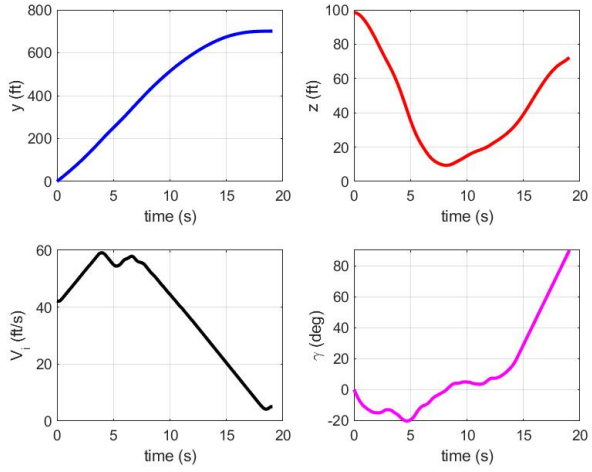

Figure 20. Time-Optimal Trajectories (Wind Frame): Forward Flight to Hover Case.

Figure 21 shows the optimal T and ϕ profiles. Figure 22 shows the idealized P and α_e profiles.

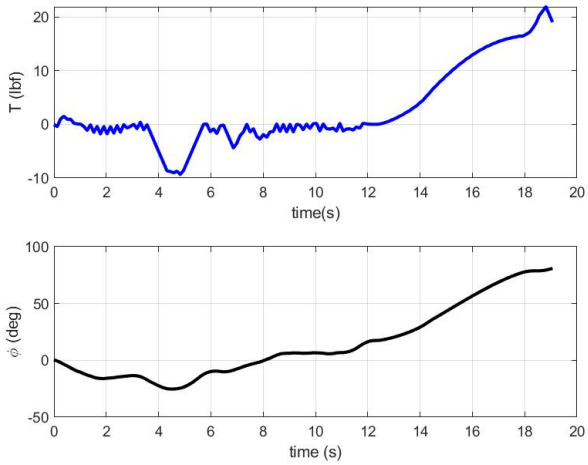

Figure 21. Prescribed Thrust and Pitch Angle Profiles for Time-Optimal Trajectories: Forward Flight to Hover Case

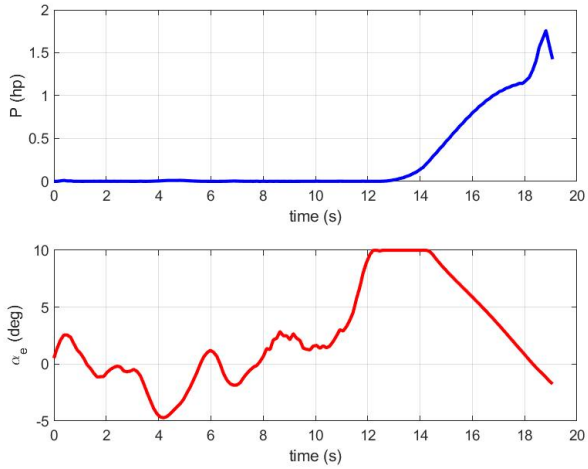

Figure 22. Prescribed Power and Stall Angle Profiles for Time-Optimal Trajectories: Forward Flight to Hover Case.

Figures 23 and 24 show the implicit wind frame and explicit body frame tracking performance for the optimal trajectories, respectively. Figure 25 shows the power and effective wing angle of attack profiles of the optimal trajectory in simulation.

From Figures 23 and 24, it can be observed that these trajectories can be tracked well. Referring to the thrust profile in Figure 21, notice the optimizer projects that the thrust will become negative during the initial descent. This fact is corroborated in the simulated power profile in Figure 25. Referring to the optimal and simulated power profiles in Figures 22 and 25, respectively, notice the discrepancy present in the power required during the beginning of the transition. As in the hover to forward flight case, this is due to the fact the the optimizer does not consider the power required to stabilize the vehicle in forward flight, thus the idealized power is lower.

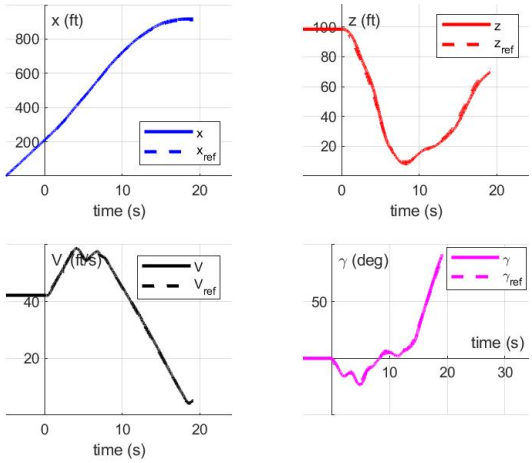

Figure 23. Tracking Performance of Time-Optimal Trajectories (Wind Frame): Forward Flight to Hover Case.

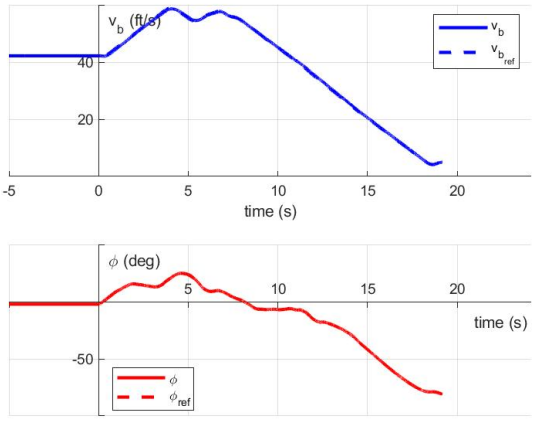

Figure 24. Tracking Performance of Time-Optimal Trajectory (Body Frame): Forward Flight to Hover Case.

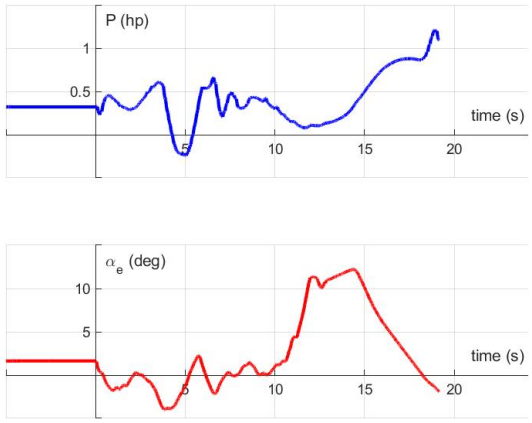

Figure 25. Power/Stall Profiles for Time-Optimal Trajectories: Forward Flight to Hover Case.

Comparison of Heuristic and Optimal Transition Trajectory Performance

Both the heuristic and the optimal trajectories for the hover to forward flight case are compared w.r.t. the optimization constraints in the interest of evaluating the optimizer. Table 2 tabulates the critical parameters of both trajectories.

Table 2. Comparison of Optimal Trajectory Constraints with Heuristic Trajectories: Hover to Forward Flight

Parameter	Constraint	Heuristic	Optimal
t_f	3s (guess)	3.2s	3.38s
P	2.01hp	1.97hp	1.89hp
α_e	10^o	4.9^o	4.27^o
$\dot{V}$	12.37 ft/s^2	11.68 ft/s^2	12.33 ft/s^2
$\dot{\gamma}$	$30^o/s$	$30^o/s$	$26.72^o/s$

From this table, it can be seen that the the optimal transition requires an additional 0.18s to complete the maneuver. However, the maneuver is completed with a lower maximum power requirement. This is likely because of the heavy emphasis placed on the power and stall constraints in the optimal trajectory. While the former was considered for the heuristically generated trajectory, the latter was not.

The heuristic and the optimal trajectories for the forward flight to hover case are similarly compared. Table 3 tabulates the critical parameters of both trajectories.

Table 3. Comparison of Optimal Trajectory Constraints with Heuristic Trajectories: Forward Flight to Hover

Parameter	Constraint	Heuristic	Optimal
t_f	40s (guess)	40s	19.17s
P	2.01hp	1.04hp	1.74hp
α_e	10^o	9.75^o	9.99^o
$\dot{V}$	4.92 ft/s^2	3.37 ft/s^2	4.78 ft/s^2
$\dot{\gamma}$	$15^o/s$	$12.05^o/s$	$14.99^o/s$
z_f	$65.6 \pm 6.56 ft$	129.42ft	72.16ft

From this table, it can be seen that the optimizer generates a forward flight to hover transition that is more that twice as fast as the heuristically generated transition while maintaining the specified terminal altitude constraint. However, the optimal transition requires significantly more power (about 67% more) than the heuristic transition and the constraints are active throughout parts of the maneuver (specifically $\dot{\gamma}$ and α_e). This increase in power is likely due to the omission of fuselage drag in the trajectory generation model, since fuselage drag is a significant source of power consumption at higher body velocities.

CONCLUSIONS

Based on the results presented above, several conclusions about the optimizer can be made. These conclusions are as follows:
1. The optimizer is capable of generating time-optimal trajectories between flight modes (hover to forward flight and vice versa) that are both feasible, while staying within all desired constraints (P, α_e, etc.).
2. Power is the primary active constraint in the transition from hover to forward flight.
3. The power constraint does not become active during the forward flight to hover case, although from what we have seen, angle of attack is the primary active constraint when there is a reduction in altitude.
4. The idealized power that is calculated from thrust does not include power required to stabilize the vehicle from transition into forward flight. In tracking, the longitudinal control inputs result in a higher power than predicted in all cases.
5. Transition from forward flight to hover is challenging particularly if a requirement for descent is added, and allowing negative thrust reduced transition flight time. While intuition and heuristic solutions are fairly effective for the transition from hover to forward flight, the descending transition to hover has the added stall condition, which is hard to intuitively avoid without extremely sub-optimal operation, so when it can be numerically solved, it provides a significant benefit (50% reduction in time).

The findings from the simulation suggest adjustments to the model can be made to increase the accuracy of the trajectories deemed feasible by the optimal trajectory solver. Potential future advancements include implementing an outer-loop framework to eliminate steady state error in altitude after transition and adding constraints that eliminate some of the oscillations in the numerical solution of the optimization problem.

Author contact:
Kristoff McIntosh, mcintk3@rpi.edu;
Jean-Paul Reddinger, jean-paul.f.reddinger.civ@mail.mil;
Di Zhao, zhaod3@rpi.edu;
Sandipan Mishra, mishrs2@rpi.edu

ACKNOWLEDGMENTS

This work is collaborative research between the CCDC Army Research Laboratory Vehicle Technology Directorate and Rensselaer Polytechnic Institute Center for Mobility and Vertical Lift (MOVE). The work was sponsored in part by the Office of Naval Research (ONR), under contract number N00014-16-1-2705, and in part under the Army/Navy/NASA Vertical Lift Research Center of Excellence (VLRCOE) Program, grant number W911W61120012, with Dr. Mahendra Bhagwat.

REFERENCES

1. Narayan, P., Wu, P., Campbell, D., and Walker, R., "An Intelligent Control Architecture for Unmanned Aerial Systems (UAS) in the National Aerospace System (NAS)," 2nd Australian Unmanned Air Vehicle Systems Conference, Melbourne, Australia, March 2007.

2. Zaludin, Z., and Harituddin, A. S. M., "Challenges and Trends of Changing from Hover to Forward Flight for a Converted Hybrid Fixed Wing VTOL UAS from Automatic Flight Control System Perspective," IEEE 9th International Conference on System Engineering and Technology, Shah Alam, Malaysia, October 2019.

3. Phillips, B., Hrishikeshavan, V., Rand, O., and Chopra, I., "Design and Development of a Scaled Quadrotor Biplane with Variable Pitch Proprotors for Rapid Payload Delivery," American Helicopter Society 72nd Annual Forum Proceedings, Palm Beach, FL, May 2016.

4. Bogdanowicz, C., Hrishikeshavan, V., and Chopra, I., "Development of a Quad-Rotor Biplane MAV with Enhanced Roll Control Authority in Fixed Wing Mode," American Helicopter Society 71st Annual Forum Proceedings, Virginia Beach, VA, May 2015.

5. Reddinger, J. P., McIntosh, K., Zhao, D., and Mishra, S., "Modeling and Trajectory Control of a Transitioning Quadrotor Biplane Tailsitter," Vertical Flight Society 75th Annual Forum Proceedings, Philadelphia, PA, May 2019.

6. Singh, R., Hirshikeshavan, V., and Sirohi, J., "Common Research Configuration for Collaborative Advancement of Scalable VTOL UAS Technologies," Vertical Flight Society 75th Annual Forum Proceedings, Philadelphia, PA, May 2019.

7. Todeschini, D., Fagiano, L., Micheli, C., and Cattano, A., "Control of vertical take off, dynamic flight and landing of hybrid drones for airborne wind energy systems," American Control Conference (ACC), Philadelphia, PA, July 2019.

8. Raj, N., Banavar, N., Ravi, Abhishek, and Kothari, M., "Attitude Control of a Novel Tailsitter: Swivelling Biplane-Qudrotor," *Journal of Guidance, Control, and Dynamics, Vol. 43, No. 3*, March, 2018.

9. Chipade, V. S., Abhishek, Kothari, M., and Chaudhari, R. R., "Systematic design methodology for development and flight testing of a variable pitch quadrotor biplane VTOL UAV for payload delivery," *Mechatronics*, Vol. 55, 2018, pp. 94 – 114. DOI: https://doi.org/10.1016/j.mechatronics.2018.08.008

10. Nogar, S. M., and Kroninger, C. M., "Development of a Hybrid Micro Air Vehicle Capable of Controlled Transition," *IEEE Robotics and Automation Letters*, Vol. 3, (3), July 2018, pp. 2269–2276. DOI: 10.1109/LRA.2018.2800797

11. Hrishikeshavan, V., Bawek, D., Rand, O., and Chopra, I., "Control of a Quad Rotor-Biplane Micro Air Vehicle

in Transition from Hover to Forward Flight," American Helicopter Society Specialists' Meeting for Unmanned Rotorcraft, Scottsdale, AZ, January 2013.

12. Swarnkar, S., Parwana, H., Kothari, M., and Abhishek, "Development of Flight Dynamics Model and Control of Biplane-Quadrotor UAV," 2018 AIAA Guidance, Navigation, and Control Conference, Kissimmee, FL, January 2018.

13. Reddinger, J. P., "Performance and Control of a Scalable Quadrotor Biplane Tailsitter," AIAA Scitech 2019 Forum, San Diego, CA, January 2019.

14. Adams, E., "Bell's New Self-Flying Cargo Drone Hauls a Heavy Load," *Wired*, September 2019. DOI: https://www.wired.com/story/bell-apt-70-cargo-drone-test-flight/

15. Weitz, L. A., "Derivation for a Point-Mass Aircraft Model Used for Fast-Time Simulation," MITRE Technical Report, November 1995.

16. Zhao, D., Krishnamurthi, J., Mishra, S., and Gandhi, F., "A Trajectory Generation Method for Time-Optimal Helicopter Shipboard Landing," American Helicopter Society 74th Annual Forum Proceedings, Fort Worth, TX, May 2018.

17. Andersson, J. A. E., Gillis, J., Horn, G., Rawlings, J. B., and Diehl, M., "CasADi – A software framework for nonlinear optimization and optimal control," *Mathematical Programming Computation*, In Press, 2018.